CONDENSED
MATTER
PHYSICS

Electronic structure and X-ray magnetic circular dichroism in the MAX phases T$_2$AlC (T=Ti and Cr) from first principles

L. V. Bekenov [ID] , S. V. Moklyak, B. F. Zhuravlev, Yu. N. Kucherenko, V. N. Antonov [ID]

G. V. Kurdyumov Institute for Metal Physics of the NAS of Ukraine, 36 Academician Vernadsky Boulevard, UA-03142 Kyiv, Ukraine

We study the electronic and magnetic properties of T$_2$AlC (T=Ti and Cr) compounds in the density-functional theory using the generalized gradient approximation (GGA) with consideration of strong Coulomb correlations (GGA+U) in the framework of the fully relativistic spin-polarized Dirac linear muffin-tin orbital (LMTO) band-structure method. The X-ray absorption spectra and X-ray magnetic circular dichroism (XMCD) at the Cr $L_{2,3}$ and Cr, Ti, and C K edges were investigated theoretically. The calculated results are in good agreement with experimental data. The effect of the electric quadrupole E_2 and magnetic dipole M_1 transitions at the Cr K edge has been investigated.

Key words: electronic structure, X-ray absorption, X-ray magnetic circular dichroism, MAX phases

1. Introduction

The M$_{n+1}$AX$_n$ (MAX) phases are layered hexagonal compounds, in which close-packed layers of M (early transition metals) are interleaved with layers of group A element (mostly IIIA and IVA), with the X-atoms (C and/or N) filling the octahedral sites between the M layers. Depending on the stoichiometry, one gets three different kinds of crystal structures classified as 211 ($n = 1$), 312 ($n = 2$) and 413 ($n = 3$), all being described by the $P6_3/mmc$ space group [1]. These carbides and nitrides have received increasing interest in recent years due to their important properties, such as low density, high elastic stiffness, thermal-shock and high-temperature oxidation resistance, good thermal and electrical conductivities, damage tolerance, and easy machinability [2–7]. These unusual properties make these compounds highly promising candidates for diverse applications in high-temperature oxidizing environments. Potential applications of the nanolaminated compounds mentioned to date range from spintronics to refrigeration, even though the research efforts have so far been focused solely on the discovery of new magnetic phases and compositions, and fundamentals of magnetic properties. However, individual properties vary from phase to phase and no systematic study of MAX phases is available in the literature. Up till now, more than 70 MAX compounds have been synthesized [8, 9], and the search is still going on. Moreover, an increasing number of scientists attempt to synthesize magnetic MAX phases [10] because magnetic MAX phases exhibit a combination of magnetic, metallic, and ceramic-like properties [11, 12], which are fascinating from the standpoints of both fundamental science and technological applications. For example, a substantial progress could happen in magnetic multilayers for magnetic recording and data storage if strong magnetism can be found in MAX phases with inherently nanolaminated compounds instead of the presently used artificially grown sandwich materials.

The ternary carbides have the properties of both metals and ceramics. Like metals, they are good thermal and electrical conductors. They are relatively soft with vickers hardness of about 2–5 GPa. Like ceramics, they are elastically stiff. Some of them (e.g., Ti$_3$SiC$_2$) also exhibit excellent high temperature mechanical properties. They are resistant to thermal shock and show unusually good damage

tolerance and exhibit excellent corrosion resistance. Above all, unlike the traditional carbides, they can be machined by conventional tools without lubricant, which makes them more technologically important for applications [6, 13]. These excellent properties make the MAX phases another class of technically important materials. Brushes in electric motors is another application of these materials. The enormous applications of this class of materials trigger us to have a better understanding of their electronic and mechanical properties.

Of special interest to this work are Ti_2AlC and Cr_2AlC carbides. The Ti_2AlC phase was first synthesized by Nowotny with co-workers [14], but its physical properties were not characterized until quite recently [2, 14–16]. The electronic structure of Ti_2AlC was calculated a number of times [17–19]. The qualitative agreement between the first and last studies is good. The ternary nanolaminated compound Cr_2AlC was discovered in 1963 by Jeitschko et al. [20]. Since that time it has been the subject of numerous studies, both experimentally [21–32] and theoretically [9–13, 22, 33–43].

In spite of many experimental and theoretical efforts to investigate the electronic structure and physical properties of the ternary MAX phases, there are still many contradictions and discrepancies among them. Many questions still remain with respect to magnetism in the the ternary nanolaminated compounds (see the review paper by Ingason et al. [1] and references therein). Schneider et al. [22] calculated the difference in cohesive energy per formula unit (f.u.) of the ferromagnetic (FM) and antiferromagnetic (AFM) configurations with reference to the nonmagnetic (NM) configuration. Based on the small total energy difference between the AFM and NM configurations as well as the comparatively small local magnetic moment (0.7 μ_B/Cr atom), the authors speculated that magnetism may be suppressed in Cr_2AlC. Sun et al. [33] also performed total energy calculations for Cr_2AlC both at AFM and NM polarized states. They found that energy difference between the two states was around 0.3 meV. Therefore, they claimed nonmagnetic ground state in Cr_2AlC. This is in agreement with the first experimental result attempting to address this point based on nuclear magnetic resonance (NMR) spectroscopy [25]. In this study, Lue et al. show, from the temperature dependence of the ^{17}Al central lines between room temperature and 77 K, that Cr_2AlC is NM in this temperature range. Ramzan et al. [43] presented the electronic and structural properties calculated by first principles GGA and GGA+U calculations of Cr_2AlC. They show that for the GGA exchange-correlation potential, the ground state of Cr_2AlC is not spin-polarized, with vanishing magnetic moments on the Cr atoms. In this case, the agreement with experiments for the equilibrium structure and the bulk modulus is not satisfactory. On the other hand, using the GGA+U approximation (with Hubbard $U = 1.95$ eV and exchange Hund coupling $J = 0.95$ eV), the calculated ground state corresponds to a FM ordering. In this case, the agreement with experiments was found to be excellent for the lattice constants and bulk modules. However, for a larger value of U (2.95 eV), the ground state magnetic order is modified, from FM (for $U = 1.95$ eV) to AFM (for $U = 2.95$ eV), and the calculated equilibrium volume was in strong disagreement with experiments. The magnitude of the magnetic moments strongly depends on the Hubbard U. Dahlqvist et al. [11, 44] state that the magnetic ground state of Cr_2AlC is in-plane AF. By comparing GGA and GGA+U results with experimental data, they found that using a $U_{eff} = U - J$ value larger than 1 eV results in structural parameters deviating strongly from experimentally observed values. The spin magnetic moments at the Cr site M_s^{Cr} were found to be equal to 0.7 μ_B [11] and 1.37 eV for the GGA and GGA+U (for $U_{eff} = 1$ eV) [44], respectively. The authors concluded that this class of Cr-based carbide MAX phases cannot be considered as strongly correlated systems since both GGA and GGA+U with $U_{eff} \leqslant 1$ eV give the calculated lattice parameters and bulk modulus close to experimentally reported values, if low-energy in-plane AFM magnetic states are considered. For larger values of the U parameter ($U_{eff} > 1$ eV), the structural parameters deviate strongly from experimentally observed values.

Soft X-ray absorption and magnetic circular dichroism in T_2AlC were measured by several authors [27, 32, 37]. Recent X-ray magnetic circular dichroism experiments performed by Jaouen et al. [32] demonstrate that Cr atoms carry a net magnetic moment in Cr_2AlC ternary phase along the c axis. The spin magnetic moment at the Cr site was found to be extremely small $M_s^{Cr} = 0.05$ μ_B, which is much smaller than the predicted values for the FM [22, 43] as well as the AFM [11, 44] solutions. SQUID experiments by Jaouen et al. [45] also produce an extremely small Cr spin magnetic moment of 0.002 μ_B in Cr_2AlC.

The aim of this paper is the theoretical study from the "first principles" of the electronic and magnetic structures and the XAS and XMCD in T_2AlC (T=Ti and Cr) carbides. The energy band structure of T_2AlC

(T=Ti and Cr) carbides is calculated within the *ab initio* approach taking into account strong electron correlations by applying a local spin-density approximation to the density functional theory supplemented by a Hubbard U term (GGA+U) [46]. The paper is organized as follows. The computational details are presented in section 2. Section 3 presents the electronic structure, XAS and XMCD spectra of T_2AlC (T=Ti and Cr) carbides at the Cr $L_{2,3}$ and Cr, Ti, and C K edges calculated in the GGA+U approximation. Theoretical results are compared to the experimental measurements. Finally, the results are summarized in section 5.

2. Crystal structure and computational details

2.1. X-ray magnetic circular dichroism

Magneto-optical (MO) effects refer to various changes in the polarization state of light upon interaction with materials possessing a net magnetic moment, including rotation of the plane of linearly polarized light (Faraday, Kerr rotation), and the complementary differential absorption of the left-hand and right-hand circularly polarized light (circular dichroism). In the near visible spectral range, these effects result from excitation of electrons in the conduction band. Near X-ray absorption edges, or resonances, magneto-optical effects can be enhanced by transitions from well-defined atomic core levels to transition symmetry selected valence states.

Within the one-particle approximation, the absorption coefficient $\mu_j^\lambda(\omega)$ for incident X-ray polarization λ and photon energy $\hbar\omega$ can be determined as the probability of electronic transitions from initial core states with the total angular momentum j to final unoccupied Bloch states

$$\mu_j^\lambda(\omega) \quad = \quad \sum_{m_j}\sum_{n\mathbf{k}} |\langle \Psi_{n\mathbf{k}}|\Pi_\lambda|\Psi_{jm_j}\rangle|^2 \delta(E_{n\mathbf{k}} - E_{jm_j} - \hbar\omega)\theta(E_{n\mathbf{k}} - E_F), \tag{2.1}$$

where Ψ_{jm_j} and E_{jm_j} are the wave function and the energy of a core state with the projection of the total angular momentum m_j; $\Psi_{n\mathbf{k}}$ and $E_{n\mathbf{k}}$ are the wave function and the energy of a valence state in the n-th band with the wave vector $\mathbf{k}$; E_F is the Fermi energy.

Π_λ is the electron-photon interaction operator in the dipole approximation

$$\Pi_\lambda = -e\boldsymbol{\alpha}\mathbf{a}_\lambda, \tag{2.2}$$

where $\boldsymbol{\alpha}$ are the Dirac matrices and $\mathbf{a}_\lambda$ is the λ polarization unit vector of the photon vector potential, with $a_\pm = 1/\sqrt{2}(1, \pm i, 0)$, $a_\parallel = (0, 0, 1)$. Here, "+" and "−" denotes, respectively, left-hand and right-hand circular photon polarizations with respect to the magnetization direction in the solid. Then, X-ray magnetic circular and linear dichroism are given by $\mu_+ - \mu_-$ and $\mu_\parallel - (\mu_+ + \mu_-)/2$, respectively. More detailed expressions of the matrix elements in the electric dipole approximation may be found in references [47–49]. The matrix elements due to magnetic dipole and electric quadrupole corrections are presented in reference [49].

2.2. General properties of spin density waves

The magnetic configuration of an incommensurate spin spiral shows the magnetic moments of certain atomic planes varying in direction. The variation has a well-defined period determined by a wave vector $\boldsymbol{q}$. When the magnetic moment is confined to the lattice sites, the magnetization $\boldsymbol{M}$ varies as [50]

$$\boldsymbol{M}(\boldsymbol{r}_n) = m_n \begin{bmatrix} \cos(\boldsymbol{q}\boldsymbol{r}_n + \phi_n)\sin(\theta_n) \\ \sin(\boldsymbol{q}\boldsymbol{r}_n + \phi_n)\sin(\theta_n) \\ \cos(\theta_n) \end{bmatrix}, \tag{2.3}$$

where the polar coordinates are used and m_n is the magnetic moment of atom n with a phase ϕ_n at the position $\boldsymbol{r}_n$. Here, we consider only planar spirals, that is, $\theta_n = \pi/2$ which also give the minimum of the total energy. The magnetization of equation (2.3) is not translationally invariant but transforms as

$$\boldsymbol{M}(\boldsymbol{r} + \boldsymbol{R}) = D(\boldsymbol{q}\boldsymbol{R})\boldsymbol{M}(\boldsymbol{r}), \tag{2.4}$$

where $\boldsymbol{R}$ is a lattice translation and D is a rotation around the z axis. A spin spiral with a magnetization in a general point $\boldsymbol{r}$ in space can be defined as a magnetic configuration which transforms according to equation (2.4). Since the spin spiral describes a spatially rotating magnetization, it can be correlated with a frozen magnon.

Since the spin spiral breaks the translational symmetry, the Bloch theorem is no longer valid. Computationally, one should use large super-cells to obtain total-energy of the spin spirals. However, when the spin-orbit interaction is neglected, spins are decoupled from the lattice and only the relative orientation of the magnetic moments is important. Then, one can define the generalized translations which contain translations in the real space and rotations in the spin space [51]. These generalized translations leave the magnetic structure invariant and lead to a generalized Bloch theorem. Therefore, the Bloch spinors can still be characterized by a $\boldsymbol{k}$ vector in the Brillouin zone, and can be written as

$$\psi_k(\boldsymbol{r}) = e^{i\boldsymbol{k}\boldsymbol{r}} \left(\begin{array}{c} e^{-i\boldsymbol{q}\boldsymbol{r}/2} u_k(\boldsymbol{r}) \\ e^{+i\boldsymbol{q}\boldsymbol{r}/2} d_k(\boldsymbol{r}) \end{array} \right). \tag{2.5}$$

The functions $u_k(\boldsymbol{r})$ and $d_k(\boldsymbol{r})$ are invariant with respect to lattice translations having the same role as for normal Bloch functions. Due to this generalized Bloch theorem, the spin spirals can be studied within the chemical unit cell and no large super-cells are needed. Though the chemical unit cell can be used, the presence of the spin spiral lowers the symmetry of the system. There remain only the space-group operations that leave invariant the wave vector of the spiral. Considering the general spin space groups, i.e., taking the spin rotations into account, the space-group operations which reverse the spiral vector together with a spin rotation of π around the x axis are symmetry operations [51].

Though the original formulation of the local-spin-density approximation of the density-functional theory permitted the noncollinear magnetic order, first-principles calculations for this aspect have begun only recently (for a review, see reference [52]). One application is the study of noncollinear ground states, for example, in γ-Fe (references [53–55]) or in frustrated antiferromagnets [56, 57]. In addition, the noncollinear formulation enables the studies of finite-temperature properties of magnetic materials. Since the dominant magnetic excitations at low temperatures are spin waves which are noncollinear by nature, it is possible to determine the magnon spectra and ultimately the Curie temperature from first principles [58–62]. The noncollinear magnetic configurations were investigated in the Heusler alloys Ni_2MnGa, Ni_2MnAl [50], $IrMnAl$ [63], Mn_3ZnC [64] and Mn_3CuN [65]. The total energies for different spin spirals were calculated and the ground-state magnetic structures were identified.

2.3. Crystal structure

The M_2AX unit cell (the space group is $P6_3/mmc$ No. 194) with two formula units per unit cell is shown in figure 1 with Wyckoff positions: M ($4f$), A ($2d$), and X ($2a$). The coordination of the M is trigonal prismatic, while that of X is octahedral. The structure possesses the layer stacking sequence of M and A atoms along the [0001] direction consisting of M_2X slabs and intercalation of planar packed A-ions. The layered stacking characteristics can be clearly illustrated in the ($1\bar{2}10$) plane, as displayed in figure 1 (b). The X atoms occupy the interstitial sites of M octahedra [see figure 1 (c)]. The crystal structure has one free internal parameter by Z_M that defines the height of the M atoms above the X sheets. The dimensionless crystallographic coordinate is $z_M = Z_M/c$. At the ideal value of $z_M = 1/12 \sim 0.0833$, the M and A planes are evenly spaced. Parameter $z_M = 0.086$ and 0.083 for Cr_2AlC and Ti_2AlC, respectively.

2.4. Calculation details

The details of the computational method are described in our previous papers [66–69] and here we only mention several aspects. Band-structure calculations were performed using the fully relativistic linear muffin-tin orbital (LMTO) method [48, 70]. This implementation of the LMTO method uses four-component basis functions constructed by solving the Dirac equation inside an atomic sphere [71]. The exchange-correlation functional of a GGA-type was used in the version of Perdew, Burke and Ernzerhof (PBE) [72]. Brillouin zone (BZ) integration was performed using the improved tetrahedron method [73]. The basis consisted of Cr and Ti s, p, d, and f and Al and C s, p, and d LMTO's.
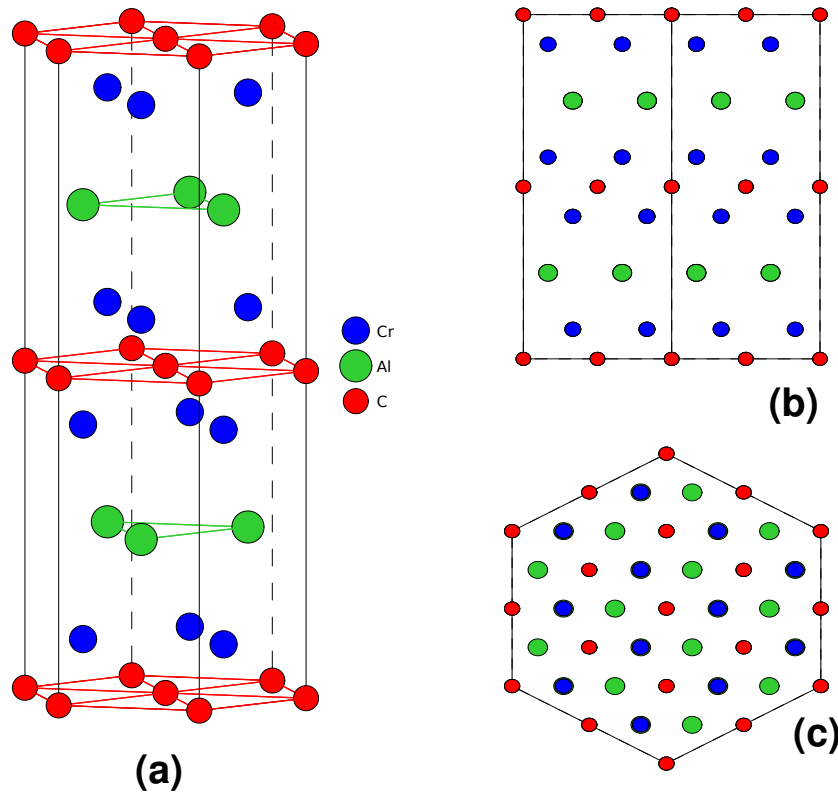
Figure 1. (Colour online) (a) Crystal structure of the Cr_2AlC (the space group is $P6_3/mmc$ No. 194). Blue spheres represent Cr atoms, green and blue spheres show Al and C atoms, respectively; (b) and (c) present arrangement of atoms on a $(1\bar{2}10)$ and (0001) planes of Cr_2AlC, respectively.

We found that the agreement between the theoretically calculated and experimentally measured XAS and XMCD spectra became much better with taking into account strong Coulomb correlations. To include the electron-electron correlations into the consideration, we used the "relativistic" generalization of the rotationally invariant version of the LSDA+U method [74] which takes into account SO coupling so that the occupation matrix of localized electrons becomes non-diagonal in spin indexes. This method is described in detail in our previous paper [74] including the procedure to calculate the screened Coulomb U and exchange J integrals, as well as the Slater integrals F^2, F^4, and F^6.

The screened Coulomb U and exchange Hund coupling J_H integrals enter the LSDA+U energy functional as external parameters and should be determined independently. These parameters can be determined from supercell LSDA calculations using Slater's transition state technique [75, 76], from constrained LSDA calculations (cLSDA) [76–80] or from the constrained random-phase approximation (cRPA) scheme [81]. Subsequently, a combined cLSDA and cRPA method was also proposed [82]. The cLSDA calculations produce $J_H = 0.95$ eV for the Cr in Cr_2AlC. It is known that the cRPA method underestimates the values of U in some cases [83]. On the other hand, the cLSDA method produces too large values of U [84]. Therefore, in our calculations we treated the Hubbard U as an external parameter and varied the effective Hubbard $U_{eff} = U - J_H$ from 0 to 3.0 eV. In the case of $U_{eff} = U - J = 0$, the effect of the GGA+U comes from non-spherical terms which are determined by F^2 and F^4 Slater integrals. This approach is similar to the orbital polarization (OP) corrections [48, 85–88]. Therefore, we use the notation GGA+OP throughout the paper for the $U_{eff} = U - J = 0$ eV approach.

The X-ray absorption and dichroism spectra were calculated taking into account the exchange splitting of the core levels. The finite lifetime of a core hole was taken into account by folding the spectra with a Lorentzian. The widths of core levels $\Gamma_{L_{2,3}}$ for Mn and Ti, and Γ_K for O were taken from reference [89]. The finite experimental resolution of the spectrometer was taken into account by a Gaussian of width 0.6 eV.

3. Electronic and magnetic structures

The theoretically calculated electronic band structure of nanolaminated ternary carbides such as Cr_2AlC and Ti_2AlC, demonstrated that the valence bands could be divided into several regions. The lowest lying group of valence states originates predominantly from the C $2s$ states. The states located at higher energy range are hybridization states of Al $3s - 3p$ orbitals. Strong pd covalent bonding states derived from Ti-C interactions dominate the adjacent higher energy range. The states just below the Fermi level contain a relatively weaker pd covalent bonding between Ti and Al. Moreover, the states near and above the Fermi level are attributed to metal-to-metal dd interactions and antibonding states.
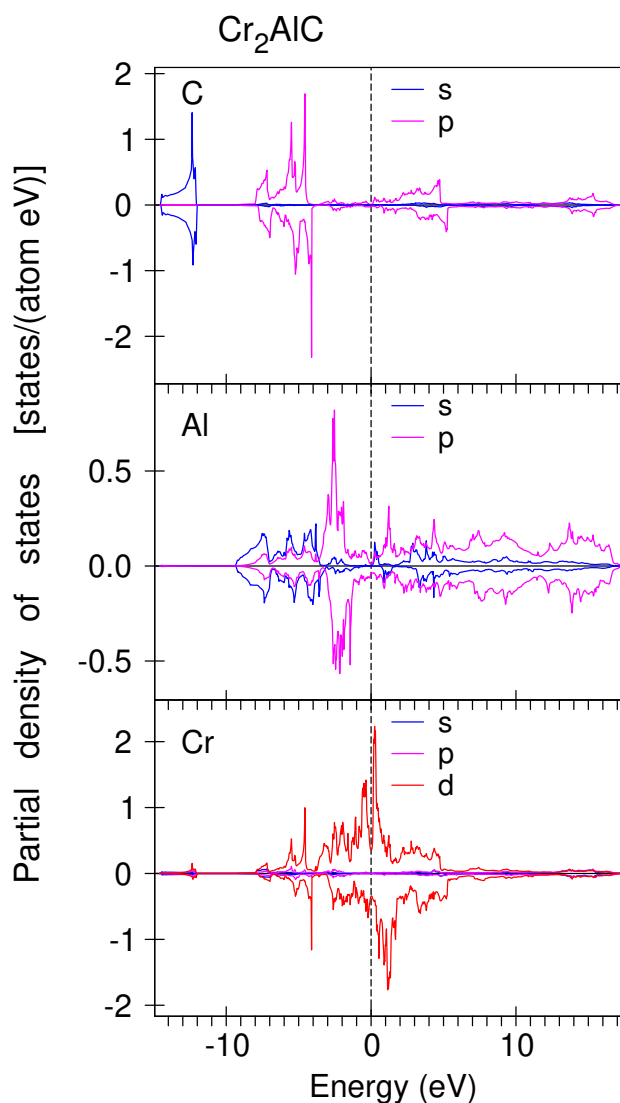

Figure 2. (Colour online) Partial density of states [in states/(atom eV)] of Cr_2AlC in the GGA approximation.

Characteristics of atomic bonding can be vividly illustrated by projected density of states (PDOS). Figures 2 and 3 show the PDOS of Cr_2AlC and Ti_2AlC for comparison. The C $2s$ states are located between -14.7 eV to -12.1 eV and -12.2 eV to -10.4 eV below the Fermi level in Cr_2AlC and Ti_2AlC, respectively. The states, which are approximately located between -5.8 and -2.8 eV below the Fermi level (E_F) in Ti_2AlC are C $2p$ states. They are well hybridized with Al sp and Ti $3d$ states. The

corresponding C $2p$ states Cr_2AlC are situated lower in energy at the -8.0 and -4.3 eV energy interval. Al $3p$ states occupy a wide energy interval from -9.0 eV to 16.0 eV and from -7.7 eV to 16.0 eV Cr_2AlC and Ti_2AlC, respectively. The major peak of the occupied Al $3p$ states associated with the pd covalent bond is situated at around -2.5 eV in Cr_2AlC and -1.0 eV in Ti_2AlC below E_F. The $3d$ orbitals of Cr atoms dominate the states near the E_F, and the contribution from Al p-derived orbitals is negligible. In comparison, the states near E_F are dominated by Ti $3d$ orbitals in Ti_2AlC, with some contribution from Al p orbitals.
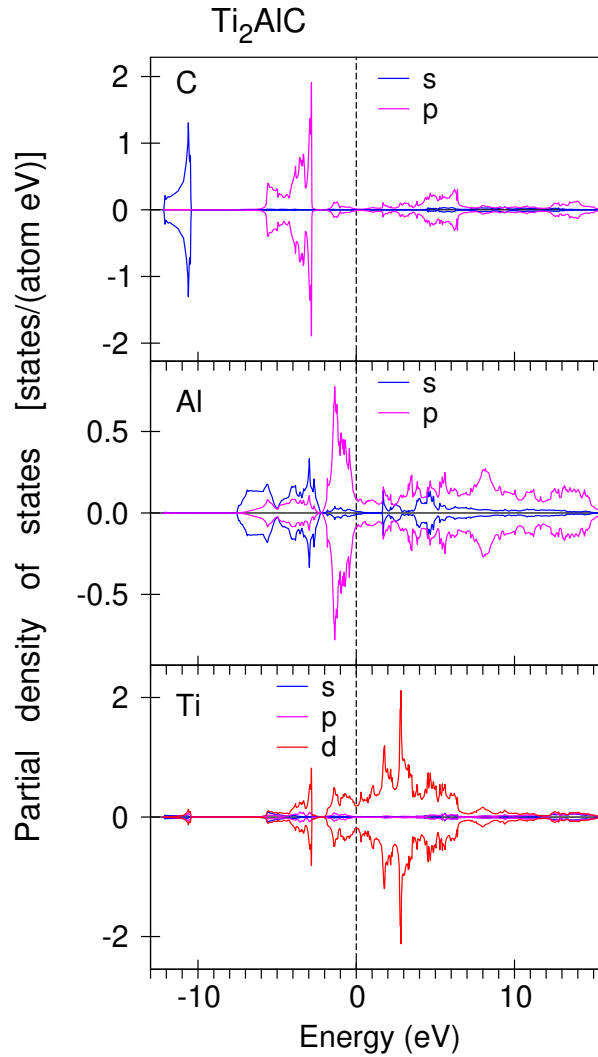

Figure 3. (Colour online) Partial density of states [in states/(atom eV)] of Ti_2AlC in the GGA approximation.

The magnitude of Cr spin and orbital magnetic moments strongly depends on the Hubbard U. The GGA approach produces the spin and orbital moments equal to 0.707 μ_B and 0.007 μ_B, respectively (see table 1). The GGA+OP approach gives slightly larger moments: $M_s^{Cr} = 0.757$ μ_B and $M_l^{Cr} = 0.009$ μ_B. For $U_{eff} = 1$ eV, 2 eV and 3 eV, the spin magnetic moments are equal to 0.973 μ_B, 2.097 μ_B, and 2.799 μ_B, respectively. These values are in good agreement with previous band structure calculations [11, 43, 44]. The orbital magnetic moments at the Cr site also strongly increased with increasing the value of Hubbard U and even change the sign for the $U_{eff} = 2$ eV and 3 eV (table 1). We found a similar dependence of the spin and orbital magnetic moments for the AFM solution as well, although the absolute values of the moments are slightly different from the FM ordering. The induced spin magnetic moments at the Al and C sites

Table 1. The theoretically calculated spin M_s, orbital M_l, and total magnetic moments (in μ_B) of Cr_2AlC for the FM solution.

Method	Atom	M_s	M_l	M_{total}
	Cr	0.707	0.007	4.134
GGA	Al	−0.015	−0.001	−0.016
	C	−0.064	0.0	−0.064
	Cr	0.757	0.009	0.766
GGA+OP	Al	−0.021	−0.001	−0.022
	C	−0.064	0.0	−0.064
	Cr	0.973	0.013	0.986
GGA+U	Al	−0.074	−0.001	−0.075
$U_{\text{eff}} = 1$ eV	C	−0.108	0.0	−0.108
	Cr	2.097	−0.030	2.067
GGA+U	Al	−0.154	−0.001	−0.155
$U_{\text{eff}} = 2$ eV	C	−0.239	−0.003	−0.242
	Cr	2.799	−0.030	2.769
GGA+U	Al	−0.196	−0.001	−0.197
$U_{\text{eff}} = 3$ eV	C	−0.357	−0.002	−0.359
LSDA reference [22]	Cr	0.70	–	–
GGA+U reference [43] $U_{\text{eff}} = 1$ eV	Cr	0.90	–	–
GGA+U reference [43] $U_{\text{eff}} = 2$ eV	Cr	2.50	–	–
exper.$_{\text{XMCD}}$ [32]	Cr	0.05	–	–
exper.$_{\text{SQIID}}$ [45]	Cr	0.002	–	–

are much smaller than at the Cr site and have an opposite direction (table 1). It is interesting to note that the spin magnetic moment at the C site is larger than the corresponding moment at the Al site. Orbital moments on both the Al and C sites are quite small.

SQUID experiments by Jaouen et al. [45] produce Cr_2AlC to be FM with extremely small Cr spin magnetic moment of 0.002 μ_B. Recent X-ray magnetic circular dichroism experiments [32] clearly demonstrate that Cr atoms carry a net magnetic moment of 0.05 μ_B in Cr_2AlC along c axis. Therefore, these experiments are in strong disagreement with all existing theoretical calculations concerning the value of the Cr spin magnetic moment and the exact nature of the magnetic ordering in Cr_2AlC ternary phase.

In order to gain an insight into the ground state magnetic configurations of Cr_2AlC, we compared the calculated total energies for different spin ordering Cr_2AlC, namely, NM, FM, and AFM phases as well as possible noncollinear magnetic (NCM) structures. We found that the total energy of the AFM_{ab} state (AFM ordering in the ab plane) is lower by 25 meV/f.u., 17 meV/f.u., and 12 meV/f.u. than those of the NM, FM, and $AFM_{[0001]}$ (AFM ordering along the c axis) states, respectively, which implies a preferable AFM phase in Cr_2AlC ordered in the ab plane. This conclusion agrees with the previous estimations by Dahlqvist et al. [11, 44]. However, this AFM_{ab} ground state is still in contradiction with the XMCD experiment by Jaouen et al. [32], because any AFM ordering produces zero net magnetization in the system. Applying the noncollinear formalism described in section 2.2 to the Cr_2AlC, we found NCM state which has a lower total energy by 6 meV/f.u. in comparison with the AFM_{ab} state. The NCM state is characterized by a canted AFM spin configuration (spin magnetic moment $M_S^{Cr} = 0.768$ μ_B in the GGA approach with the polar angles equal to $\theta^{Cr_1} = 91.7°$, $\phi^{Cr_1} = 0°$ and $\theta^{Cr_2} = 91.4°$, $\phi^{Cr_1} = 180°$). Such a AFM configuration with the spins slightly canted out of the (a, b) plane produces a small projection of the Cr spin magnetic moment along the c axis of around 0.047 μ_B, which is in excellent agreement with the estimation by Jaouen et al. [32] of 0.05 μ_B using the XMCD measurements and sum rules. Strictly speaking, we do not have AFM ordering in the (a, b) plane but rather ferrimagnetic (FiM) ordering with

a small net magnetization of 0.005 μ_B in the plane.

We found that Ti_2AlC is very close to NM ground state. Though titanium is in the Ti^{2+} state (d^2), the spin magnetic moment at the Ti as well as at Al sites is less than 10^{-4} μ_B.

4. X-ray absorption and XMCD spectra

Figure 4 presents the X-ray absorption spectra (open circles) at the Cr $L_{2,3}$ edges (top panel) in Cr_2AlC measured at 4.2 K [32] with a 6 T exteranal magnetic field compared with the theoretically calculated ones (full blue curve). Since the pure Cr L_{23} edges are structureless, the existence of these fine structures shows that the chromium is not in a pure metallic state in Cr_2AlC, a well-known fact from previous band structure calculations related to MAX phases [90]. They all have a mixture of covalent, metallic and ionic bonds.
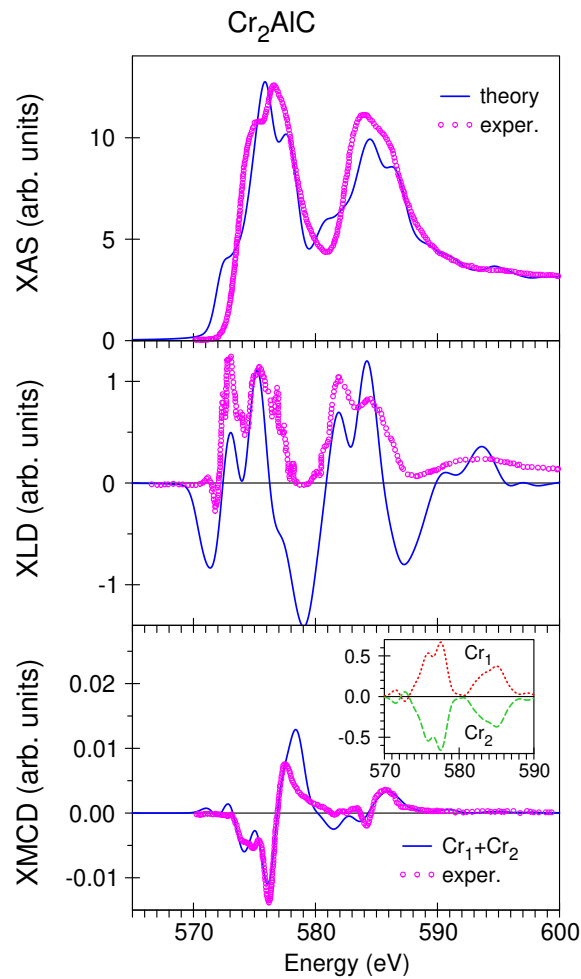

Figure 4. (Colour online) Top panel: the X-ray absorption spectra (open circles) at the Cr $L_{2,3}$ edges in Cr_2AlC measured at 4.2 K [32] with a 6 T magnetic compared with the theoretically calculated ones (full blue curve) calculated in the GGA approach; Middle panel: the theoretically calculated (full blue curve) and experimentally measured (open circles) [32] X-ray linear dichroism spectra; lower panel: the XMCD experimental spectra (open circles) of Cr_2AlC at the Cr $L_{2,3}$ edges and the theoretically calculated one (full blue line); the onset shows the XMCD spectra at the Gr $L_{2,3}$ edges separately from the Cr_1 and Cr_2 sites.

One can observe a well separated double structure at the top of both L_3 and L_2 edges. These fine

structures are well reproduced by a band structure calculation, although the theory produces inverse relative intensities between low and high energy peaks in comparison with the experimentally observed ones in the L_3 XAS spectrum. It is interesting to note that the model multiple scattering calculations performed with the FEFF [91, 92] code by Jaouen et al. [32] show the same inversion in the relative intensities as obtained by us.

Figure 4 (middle panel) shows the theoretically calculated (full blue curve) and experimentally measured (open circles) [32] X-ray linear dichroism spectra. The theory reproduces the energy position of all the fine structures quite well, although the negative peaks at 571 eV, 578 eV, and 587 eV are much lower in theory than in the experiment.

The XMCD experimental spectra (open circles) of Cr_2AlC at the Cr $L_{2,3}$ edges and the theoretically calculated spectrum (full blue line) are presented in the lower panel of figure 4. For the experimental geometry used in reference [32] it follows that the electric field, $\mathbf{E}$, of the incident X-ray beam is parallel to the (a, b) plane of the MAX phase. In that case, XAS measurements mainly probe the unoccupied Cr $3d_{xy}$, $3d_{xz}$, $3d_{yz}$ and $3d_{x^2-y^2}$ in-plane orbitals, as well as a much smaller $p \rightarrow s$ contribution. The X-ray dichroism at the Cr $L_{2,3}$ edges is quite small due to cancellation signals from Cr_1 and Cr_2 sites (see the insert in the lower panel of figure 4). The agreement between the theory and experiment is quite good although the intensity of the major positive peak at 578 eV is slightly overestimated in the theory.
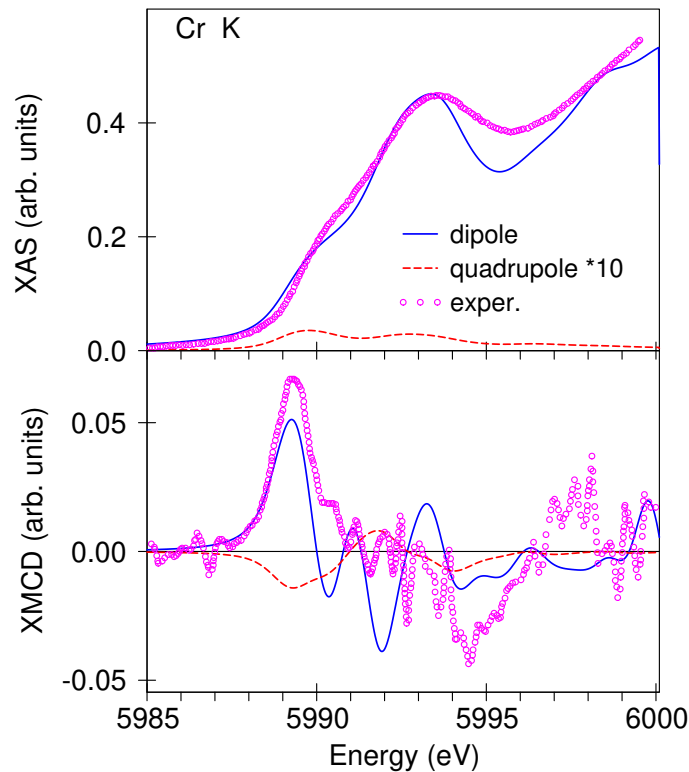

Figure 5. (Colour online) Top panel: the X-ray absorption spectrum (open circles) at the Cr K edge in Cr_2AlC measured at 2.2 K [32] and external magnetic field of 10 T with the theoretically calculated ones in the GGA approach taking into account only dipole $1s \rightarrow 2p$ transitions (full blue curve) and quadrupole $1s \rightarrow 3d$ transitions (dashed red curve) multiply by factor 10; lower panel: the XMCD experimental spectrum (open circles) of Cr_2AlC at the Cr K edge and the theoretically calculated ones in dipole approximation (full blue line) and quadrupole transitions (dashed red curve) multiply by factor 10.

We found that both the GGA and GGA+U with $U_{eff} \leqslant 1$ eV give the calculated XAS and XMCD spectra close to experimentally measured ones. For larger values of the U-parameter ($U_{eff} > 1$ eV), the theoretically calculated XMCD spectra deviate strongly from experimentally observed spectra. Therefore, this class of Cr-based carbide MAX phases cannot be considered as strongly correlated systems. A similar

conclusion was also drawn by Dahlqvist et al. [11, 44] based on the calculations of lattice parameters and bulk modulus in the Cr_2AlC, Cr_2GaC and Cr_2GeC.

Figure 5 presents the X-ray absorption spectrum (open circles) at the Cr K edge (top panel) in Cr_2AlC measured at 2.2 K [32] with magnetic field of 10 T compared with the theoretically calculated ones (full blue curve). The XAS spectrum consists of a major peak at 5993.4 eV followed by a local minimum at 5996.0 eV and a low energy shoulder at 5989.3 eV. The theory well reproduces the energy position and shape of the fine structures. It is worth noticing that the low energy shoulder at 5989.3 eV is usually attributed to the quadrupolar E_2 ($1s \rightarrow 3d$) transitions [32, 92]. We investigate the effect of the electric quadrupole E_2 and magnetic dipole M_1 transitions. We found that the M_1 transitions are extremely small in comparison with the E_2 transitions and can be neglected. The E_2 transitions indeed contribute to the low energy shoulder at 5989.3 eV as well as to the major peak at 5993.4 eV, although the quadrupolar E_2 transitions are by two orders of magnitude smaller than the electric dipole transitions E_1 (see a red dashed curve at the upper panel of figure 5). Therefore, the low energy shoulder reflects the energy distribution of C N_p partial DOS (figure 2).

The lower panel shows the XMCD experimental spectrum (open circles) of Cr_2AlC at the Cr K edge and the theoretically calculated ones in the dipole approximation (full blue line). The dashed-dotted lines show the contribution from the quadrupole E_2 ($1s \rightarrow 3d$) transitions multiplied by a factor of 10. Again, the contribution of the quadrupolar E_2 ($1s \rightarrow 3d$) transitions to the Cr K XMCD spectrum is very small. The theory well reproduces the energy position and the intensity of the major positive peak at 5989.3 eV, while other fine structures are reproduced with less accuracy, although it is hard to achieve an ideal agreement with the experimental measurements with such a very weak detected XMCD signal.
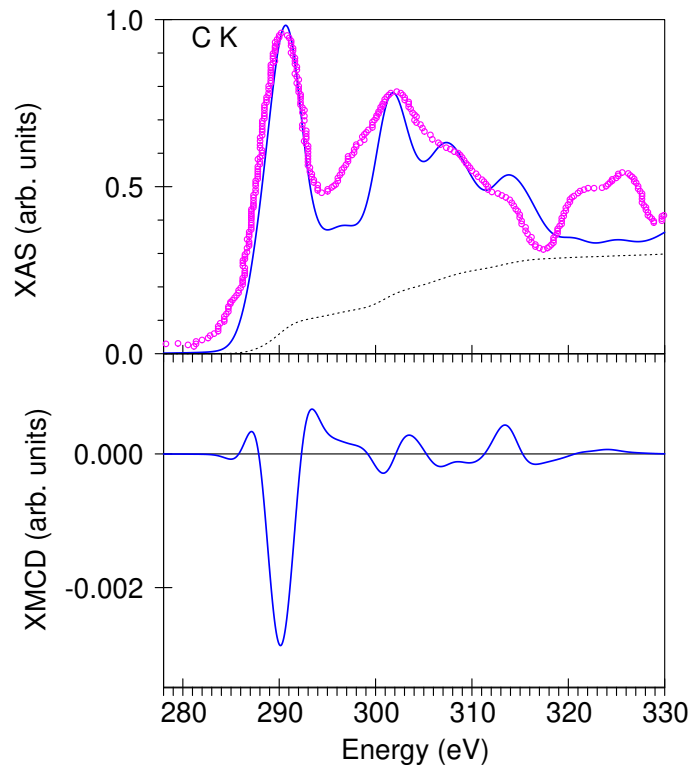

Figure 6. (Colour online) Top panel: the X-ray absorption spectrum (open circles) at the C K edge in Cr_2AlC measured at 4.2 K [27] with a 6 T magnetic compared with the theoretically calculated one (full blue curve) in the GGA approach; lower panel: the theoretically calculated XMCD spectrum of Cr_2AlC at the C K edge.

Figure 6 presents the X-ray absorption spectrum (open circles) at the C K edge (top panel) in Cr_2AlC measured by Lin et al. [27] compared with the theoretically calculated ones (full blue curve). Our

band structure calculations well reproduce the energy position of all fine structures of the experimental C *K* XAS spectrum. Shindo and Oikawa [93] investigated the XAS spectra of diamond, graphite, and amorphous carbon. They reported that a XAS peak at 291 eV indicated a strong σ bonding state for C. On the other hand, a π bonding state of carbon was distinguished by a π^* peak at ~ 284 eV in the XAS spectra [27, 93]. In the experimentally measured C *K* edge for Cr_2AlC, the peak was located at about 290 eV, which implies that the Cr–C bond in Cr_2AlC is a strong σ bonding [27].

Figure 6 (bottom panel) presents the theoretically calculated XMCD spectrum at the C *K* edge in Cr_2AlC. Due to very small spin and orbital magnetic moments at the C site (see table 1), one would expect a quite small dichroism at this edge with major negative peak at 291 eV. The experimental measurements of the XMCD spectrum at the C *K* edge are highly desirable.

Spin and orbital magnetic moments in Ti_2AlC are very small at the Ti and C sites. Therefore, the XMCD spectra at these edges are not detected yet. The theoretically calculated XMCD spectra (not shown) are three orders of magnitude smaller than their XAS spectra.

Figure 7 shows the X-ray absorption spectra (open circles) at the Ti *K* (upper panel) [37] and C *K* (lower panel) [37] edges in Ti_2AlC compared to the theoretically calculated spectra (full blue curves). The theory quite well reproduces the experimental spectra.
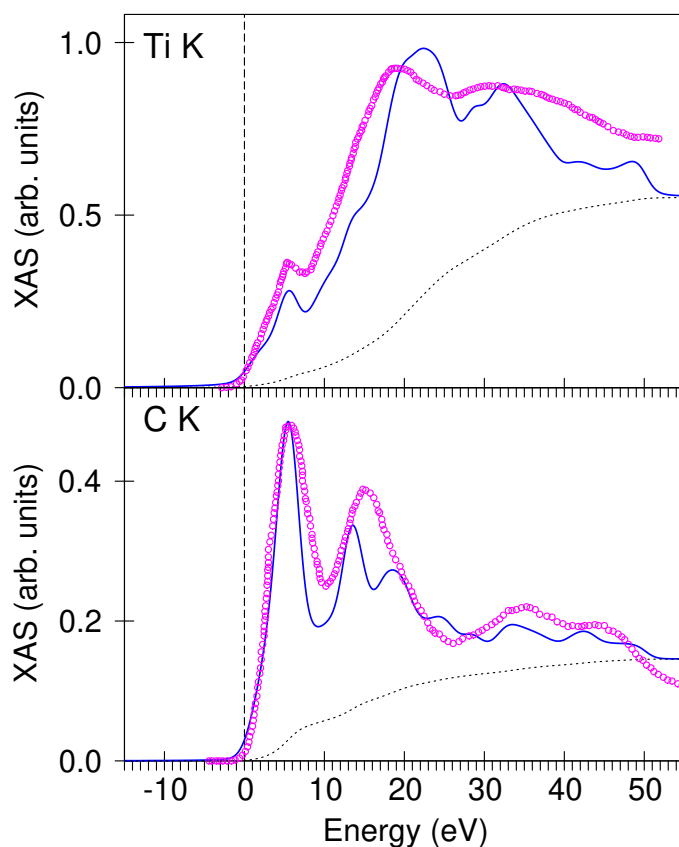

Figure 7. (Colour online) top panel: the experimentally measured [37] X-ray absorption spectrum at Ti *K* edge in Ti_2AlC (magenta circles) and theoretically calculated (full blue curve) in the GGA approach; lower panel: the experimentally measured [37] X-ray absorption spectrum at C *K* edge in Ti_2AlC (magenta circles) and theoretically calculated (full blue curve) in the GGA approach.

The energy position of a major low energy peak at the C *K* edge coincides with the low energy shoulder of Ti *K* XAS spectrum at 4 eV above the edge indicating a strong Ti *d* – C *P* σ bonding in Ti_2AlC.

5. Summary

The electronic and magnetic structures and X-ray magnetic circular dichroism of the MAX 211 compounds Cr_2AlC and Ti_2AlC were investigated theoretically within GGA and GGA+U approaches in the framework of the fully relativistic spin-polarized Dirac LMTO band-structure method.

We found the non-collienear magnetic state as a ground state in Cr_2AlC which is characterized by a canted AFM spin configuration (spin magnetic moment $M_S^{Cr} = 0.768$ μ_B in the GGA approach with the polar angles equal to $\theta^{Cr_1} = 91.7°$, $\phi^{Cr_1} = 0°$ and $\theta^{Cr_2} = 91.4°$, $\phi^{Cr_1} = 180°$). Such AFM configuration with spins is slightly canted out of the (a, b) plane and produces a small projection of the Cr spin magnetic moment along the c axis of around 0.047 μ_B, which is in excellent agreement with the estimation by Jaouen et al. [32] of 0.05 μ_B using the XMCD measurements and sum rules. There is a ferrimagnetic ordering in the (a, b) plane with net magnetization of 0.005 μ_B.

We have studied an X-ray magnetic circular dichroism at the Cr $L_{2,3}$ and Cr, C, and Ti K edges in Cr_2AlC and Ti_2AlC. The calculations show a good agreement with the experimental measurements. We cannot validate the significance for using the LSDA(GGA)+U methods for the study of magnetic MAX phases since both GGA and GGA+U with $U_{eff} \leqslant 1$ eV give the calculated XAS and XMCD spectra close to the experimentally measured ones. Therefore, this class of Cr-based carbide MAX phases cannot be considered as strongly correlated systems.

References

1. Ingason A. S., Dahlqvist M., Rosen J., J. Phys.: Condens. Matter, 2016, **28**, 433003, doi:10.1088/0953-8984/28/43/433003.
2. Barsoum M. W., Prog. Solid State Chem., 2000, **28**, 201, doi:10.1016/S0079-6786(00)00006-6.
3. Barsoum M. W., El-Raghy T., Am. Sci., 2001, **89**, 334.
4. Wang J., Zhou Y., Annu. Rev. Mater. Res., 2009, **39**, 415, doi:10.1146/annurev-matsci-082908-145340.
5. Scabarozi T. H., Amini S., Leaffer O., Ganguly A., Gupta S., Tambussi W., Clipper S., Spanier J. E., Barsoum M. W., Hettinger J. D., Lofland S. E., J. Appl. Phys., 2009, **105**, 013543, doi:10.1063/1.3021465.
6. Barsoum M. W., In: Ceramics Science and Technology, Riedel R., Chen I. W. (Eds.), Wiley, New York, 2010, 299.
7. Eklund P., Beckers M., Jansson U., Högberg H., Hultman H., Thin Solid Films, 2010, **518**, 1851, doi:10.1016/j.tsf.2009.07.184.
8. Mo Y., Rulis P., Ching W. Y., Phys. Rev. B, 2012, **86**, 165122, doi:10.1103/PhysRevB.86.165122.
9. Li N., Mo Y., Ching W. Y., J. Appl. Phys., 2013, **114**, 183503, doi:10.1063/1.4829485.
10. Dahlqvist M., Alling B., Abrikosov I. A., Rosén J., Phys. Rev. B, 2011, **84**, 220403(R), doi:10.1103/PhysRevB.84.220403.
11. Dahlqvist M., Alling B., Rosén J., J. Appl. Phys., 2013, **113**, 216103, doi:10.1063/1.4808239.
12. Mockute A., Dahlqvist M., Emmerlich J., Hultman L., Schneider J. M., Persson P. O. Å., Rosen J., Phys. Rev. B, 2013, **87**, 094113, doi:10.1103/PhysRevB.87.094113.
13. Sun W., Luo W., Ahuja R., J. Mater. Sci., 2012, **47**, 7615, doi:10.1007/s10853-012-6609-6.
14. Jeitschko W., Nowotny H., Benesovsky F., J. Less-Common Met., 1964, **7**, 133, doi:10.1016/0022-5088(64)90055-4.
15. Sayers D. E., Stern E. A., Lytle F. W., Phys. Rev. Lett., 1971, **27**, 1204, doi:10.1103/PhysRevLett.27.1204.
16. Salama I., El-Raghy T., Barsoum M. W., J. Alloys Compd., 2002, **347**, 271, doi:10.1016/S0925-8388(02)00756-9.
17. Matar S. F., Petitcorps Y. L., Etourneau J., J. Mater. Chem., 1997, **7**, 99, doi:10.1039/A605113H.
18. Hug G., Fries E., Phys. Rev. B, 2002, **65**, 113104, doi:10.1103/PhysRevB.65.113104.
19. Zhou Y., Sun Z., Phys. Rev. B, 2000, **61**, 12570, doi:10.1103/PhysRevB.61.12570.
20. Jeitschko W., Nowotny H., Benesovsky F., Monatsh. Chem., 1963, **94**, 672, doi:10.1007/BF00913068, (in German).
21. Nowotny H., Prog. Solid State Chem., 1971, **5**, 27, doi:10.1016/0079-6786(71)90016-1.
22. Schneider J. M., Sun Z., Mertens R., Uestel F., Ahuja R., Solid State Commun., 2004, **130**, 445, doi:10.1016/j.ssc.2004.02.047.
23. Hettinger J. D., Lofland S. E., Finkel P., Meehan T., Palma J., Harrell K., Gupta S., Ganguly A., El-Raghy T., Barsoum M. W., Phys. Rev. B, 2005, **72**, 115120, doi:10.1103/PhysRevB.72.115120.

24. Manoun B., Gulve R. P., Saxena S. K., Gupta S., Barsoum M. W., Zha C. S., Phys. Rev. B, 2006, **73**, 024110, doi:10.1103/PhysRevB.73.024110.

25. Lue C. S., Lin J. Y., Xie B. X., Phys. Rev. B, 2006, **73**, 035125, doi:10.1103/PhysRevB.73.035125.

26. Lofland S. E., Hettinger J. D., Meehan T., Bryan A., Finkel P., Gupta S., Barsoum M. W., Hug G., Phys. Rev. B, 2006, **74**, 174501, doi:10.1103/PhysRevB.74.174501.

27. Lin Z., Zhuo M., Zhou Y., Li M., Wang J., J. Appl. Phys., 2006, **99**, 076109, doi:10.1063/1.2188074.

28. Schneider J. M., Sigumonrong D. P., Music D., Walter C., Emmerlich J., Iskandar R., Mayer J., Scr. Mater., 2007, **57**, 1137, doi:10.1016/j.scriptamat.2007.08.006.

29. Li J. J., Hu L. F., Li F. Z., Li M. S., Zhou Y. C., Surf. Coat. Technol., 2010, **204**, 3838, doi:10.1016/j.surfcoat.2010.04.067.

30. Abdulkadhim A., Baben M., Takahashi T., Schnabel V., Hans M., Polzer C., Polcik P., Schneider J. M., Surf. Coat. Technol., 2011, **206**, 599, doi:10.1016/j.surfcoat.2011.06.003.

31. Amini S., Zhou A., Gupta S., DeVillier A., Finkel P., Barsoum M. W., J. Mater. Res., 2008, **23**, 2157, doi:10.1557/JMR.2008.0262.

32. Jaouen M., Bugnet M., Jaouen N., Ohresser P., Mauchamp V., Cabioch T., Rogalev A., J. Phys.: Condens. Matter, 2014, **26**, 176002, doi:10.1088/0953-8984/26/17/176002.

33. Sun Z., Ahuja R., Li S., Schneider J. M., Appl. Phys. Lett., 2003, **83**, 899, doi:10.1063/1.1599038.

34. Lofland S. E., Hettinger J. D., Harrell K., Finkel P., Gupta S., Barsoum M. W., Hug G., Appl. Phys. Lett., 2004, **84**, 508, doi:10.1063/1.1641177.

35. Wang J., Zhou Y., Phys. Rev. B, 2004, **69**, 214111, doi:10.1103/PhysRevB.69.214111.

36. Sun Z., Music D., Ahuja R., Li S., Schneider J. M., Phys. Rev. B, 2004, **70**, 092102, doi:10.1103/PhysRevB.70.092102.

37. Hug G., Jaouen M., Barsoum M. W., Phys. Rev. B, 2005, **71**, 024105, doi:10.1103/PhysRevB.71.024105.

38. Music D., Schneider J. M., JOM, 2007, **59**, 60, doi:10.1007/s11837-007-0091-7.

39. Bouhemadou A., Appl. Phys. A, 2009, **96**, 959, doi:10.1007/s00339-009-5106-5.

40. Zhou W., Liu L., Wu P., J. Appl. Phys., 2009, **106**, 033501, doi:10.1063/1.3187912.

41. Jia G., Yang L., Physica B, 2010, **405**, 4561, doi:10.1016/j.physb.2010.08.038.

42. Du Y. L., Sun Z. M., Hashimoto H., Barsoum M. W., J. Appl. Phys., 2011, **109**, 063707, doi:10.1063/1.3562145.

43. Ramzan M., Lebegue S., Ahuja R., Phys. Status Solidi RRL, 2011, **5**, 122, doi:10.1002/pssr.201004508.

44. Dahlqvist M., Alling B., Rosen J., J. Phys.: Condens. Matter, 2015, **27**, 095601, doi:10.1088/0953-8984/27/9/095601.

45. Jaouen M., Chartier P., Cabioch T., Mauchamp V., André G., Viret M., J. Am. Ceram. Soc., 2013, **96**, 3872, doi:10.1111/jace.12635.

46. Anisimov V. I., Zaanen J., Andersen O. K., Phys. Rev. B, 1991, **44**, 943, doi:10.1103/PhysRevB.44.943.

47. Guo G. Y., Ebert H., Temmerman W. M., Durham P. J., Phys. Rev. B, 1994, **50**, 3861, doi:10.1103/PhysRevB.50.3861.

48. Antonov V., Harmon B., Yaresko A., Electronic Structure and Magneto-Optical Properties of Solids, Kluwer, Dordrecht, 2004.

49. Arola E., Horne M., Strange P., Winter H., Szotek Z., Temmerman W. M., Phys. Rev. B, 2004, **70**, 235127, doi:10.1103/PhysRevB.70.235127.

50. Enkovaara J., Ayuela A., Jalkanen J., Nordström L., Nieminen R. M., Phys. Rev. B, 2003, **67**, 054417, doi:10.1103/PhysRevB.67.054417.

51. Sandratskii L. M., J. Phys.: Condens. Matter, 1991, **3**, 8565, doi:10.1088/0953-8984/3/44/004.

52. Sandratskii L. M., Adv. Phys., 1998, **47**, 91, doi:10.1080/000187398243573.

53. Sandratskii L. M., Kübler J., J. Phys.: Condens. Matter, 1992, **4**, 6927, doi:10.1088/0953-8984/4/33/007.

54. Bylander D. M., Kleinman L., Phys. Rev. B, 1999, **59**, 6278, doi:10.1103/PhysRevB.59.6278.

55. Knöpfle K., Sandratskii L. M., Kübler J., Phys. Rev. B, 2000, **62**, 5564, doi:10.1103/PhysRevB.62.5564.

56. Kurz Ph., Bihlmayer G., Hirai K., Blügel S., Phys. Rev. Lett., 2001, **86**, 1106, doi:10.1103/PhysRevLett.86.1106.

57. Hobbs D., Hafner J., J. Phys.: Condens. Matter, 2000, **12**, 7025, doi:10.1088/0953-8984/12/31/304.

58. Antropov V. P., Katsnelson M. I., van Schilfgaarde M., Harmon B. N., Phys. Rev. Lett., 1995, **75**, 729–732, doi:10.1103/PhysRevLett.75.729.

59. Rosengaard N. M., Johansson B., Phys. Rev. B, 1997, **55**, 14975, doi:10.1103/PhysRevB.55.14975.

60. Uhl M., Kübler J., Phys. Rev. Lett., 1996, **77**, 334, doi:10.1103/PhysRevLett.77.334.

61. Halilov S. V., Eschrig H., Perlov A. Y., Oppeneer P. M., Phys. Rev. B, 1998, **58**, 293, doi:10.1103/PhysRevB.58.293.

62. Pajda M., Kudrnovský J., Turek I., Drchal V., Bruno P., Phys. Rev. B, 2001, **64**, 174402, doi:10.1103/PhysRevB.64.174402.

63. Antonov V. N., Harmon B. N., Yaresko A. N., Bekenov L. V., Shpak A. P., Phys. Rev. B, 2006, **73**, 094445,

doi:10.1103/PhysRevB.73.094445.

64. Antonov V. N., Harmon B. N., Yaresko A. N., Shpak A. P., Phys. Rev. B, 2007, **75**, 165114, doi:10.1103/PhysRevB.75.165114.

65. Antonov V. N., Bekenov L. V., Low Temp. Phys., 2014, **40**, 641, doi:10.1063/1.4887062.

66. Leonov I., Yaresko A. N., Antonov V. N., Schwingenschlögl U., Eyert V., Anisimov V. I., J. Phys.: Condens. Matter, 2006, **18**, 10955–10964, doi:10.1088/0953-8984/18/48/022.

67. Antonov V. N., Harmon B. N., Yaresko A. N., Shpak A. P., Phys. Rev. B, 2007, **75**, 184422, doi:10.1103/PhysRevB.75.184422.

68. Antonov V. N., Yaresko A. N., Jepsen O., Phys. Rev. B, 2010, **81**, 075209, doi:10.1103/PhysRevB.81.075209.

69. Ruck B. J., Trodahl H. J., Richter J. H., Cezar J. C., Wilhelm F., Rogalev A., Antonov V. N., Le B. D., Meyer C., Phys. Rev. B, 2011, **83**, 174404, doi:10.1103/PhysRevB.83.174404.

70. Andersen O. K., Phys. Rev. B, 1975, **12**, 3060, doi:10.1103/PhysRevB.12.3060.

71. Nemoshkalenko V. V., Krasovskii A. E., Antonov V. N., Antonov Vl. N., Fleck U., Wonn H., Ziesche P., Phys. Status Solidi B, 1983, **120**, 283–296, doi:10.1002/pssb.2221200130.

72. Perdew J. P., Burke K., Ernzerhof M., Phys. Rev. Lett., 1996, **77**, 3865–3868, doi:10.1103/PhysRevLett.77.3865.

73. Blöchl P. E., Jepsen O., Andersen O. K., Phys. Rev. B, 1994, **49**, 16223, doi:10.1103/PhysRevB.49.16223.

74. Yaresko A. N., Antonov V. N., Fulde P., Phys. Rev. B, 2003, **67**, 155103, doi:10.1103/PhysRevB.67.155103.

75. Anisimov V. I., Gunnarsson O., Phys. Rev. B, 1991, **43**, 7570, doi:10.1103/PhysRevB.43.7570.

76. Solovyev I. V., Dederichs P. H., Anisimov V. I., Phys. Rev. B, 1994, **50**, 16861–16871, doi:10.1103/PhysRevB.50.16861.

77. Dederichs P. H., Blügel S., Zeller R., Akai H., Phys. Rev. Lett., 1984, **53**, 2512, doi:10.1103/PhysRevLett.53.2512.

78. Pickett W. E., Erwin S. C., Ethridge E. C., Phys. Rev. B, 1998, **58**, 1201–1209, doi:10.1103/PhysRevB.58.1201.

79. Cococcioni M., de Gironcoli S., Phys. Rev. B, 2005, **71**, 035105, doi:10.1103/PhysRevB.71.035105.

80. Nakamura K., Arita R., Yoshimoto Y., Tsuneyuki S., Phys. Rev. B, 2006, **74**, 235113, doi:10.1103/PhysRevB.74.235113.

81. Aryasetiawan F., Imada M., Georges A., Kotliar G., Biermann S., Lichtenstein A. I., Phys. Rev. B, 2004, **70**, 195104, doi:10.1103/PhysRevB.70.195104.

82. Solovyev I. V., Imada M., Phys. Rev. B, 2005, **71**, 045103, doi:10.1103/PhysRevB.71.045103.

83. Antropov V. P., Antonov V. N., Bekenov L. V., Kutepov A., Kotliar G., Phys. Rev. B, 2014, **90**, 054404, doi:10.1103/PhysRevB.90.054404.

84. Aryasetiawan F., Karlsson K., Jepsen O., Schönberger U., Phys. Rev. B, 2006, **74**, 125106, doi:10.1103/PhysRevB.74.125106.

85. Brooks M. S. S., Physica B+C, 1985, **130**, 6, doi:10.1016/0378-4363(85)90170-6.

86. Eriksson O., Brooks M. S. S., Johansson B., Phys. Rev. B, 1990, **41**, 7311(R), doi:10.1103/PhysRevB.41.7311.

87. Severin L., Brooks M. S. S., Johansson B., Phys. Rev. Lett., 1993, **71**, 3214, doi:10.1103/PhysRevLett.71.3214.

88. Mavromaras A., Sandratskii L., Kübler J., Solid State Commun., 1998, **106**, 115, doi:10.1016/S0038-1098(98)00052-0.

89. Campbell J. L., Papp T., At. Data Nucl. Data Tables, 2001, **77**, 1–56, doi:10.1006/adnd.2000.0848.

90. Lin Z., Zhou Y., Li M., J. Mater. Sci. Technol., 2007, **23**, 721.

91. Abadias G., Koutsokeras L. E., Guerin Ph., Patsalas P., Thin Solid Films, 2009, **518**, 1532, doi:10.1016/j.tsf.2009.07.183.

92. Rehr J., Albers R. C., Rev. Mod. Phys., 2000, **72**, 621, doi:10.1103/RevModPhys.72.621.

93. Shindo D., Oikawa T., Analytical Electron Microscopy for Materials Science, Kyoritsu Shuppan, Tokyo, 1999.

Електронна структура та рентгенівський магнітний циркулярний дихроїзм у MAX фазах T$_2$AlC (T=Ti або Cr), визначені з перших принципів

Л. В. Бекеньов, С. В. Мокляк, Б. Ф. Журавльов, Ю. Кучеренко, В. М. Антонов

Інститут металофізики ім. Г. В. Курдюмова НАН України, бульвар Академіка Вернадського, 36, UA-03142 Київ, Україна

Ми вивчаємо електронні та магнітні властивості сполук T$_2$AlC (T=Ti та Cr) в рамках теорії функціоналу густини з використанням узагальненого градієнтного наближення (GGA) з урахуванням сильних кулонівських кореляцій (GGA+U), розраховуючи зонну структуру в формалізмі повністю релятивістського спін-поляризованого методу діраківських лінійних MT-орбіталей (LMTO). Теоретично досліджені рентгенівські спектри поглинання та рентгенівський магнітний циркулярний дихроїзм (XMCD) на Cr $L_{2,3}$ та Cr, Ti, C K краях поглинання. Результати розрахунків добре узгоджуються з експериментальними даними. Досліджено вплив електричного квадрупольного E_2 та магнітного дипольного M_1 переходів на Cr K краю поглинання.

Ключові слова: *електронна структура, спектри рентгенівського поглинання, рентгенівський магнітний циркулярний дихроїзм, MAX фази*